

Entropy-modulated atomic ripple texturing in two-dimensional transition metal carbonitrides

Received: 3 September 2024

Accepted: 6 June 2025

Published online: 01 July 2025

 Check for updatesMinmin Liu^{1,2}, Liting Yang^{1,2}, Zhengchen Wu^{1,2}, Guanyu Chen¹, Xiangyu Wang¹, Xiaofen Yang¹, Guisheng Liang¹ & Renchao Che¹  

Periodically atomic displacement in two-dimensional (2D) ripple texturing offers a promising route for selective modulation of local potential, crucial for advanced electronic engineering. However, in 2D transition metal carbonitrides (MXenes), the construction and regulation of atomic ripples to control electronic properties meet substantial challenges due to the difficulty in tailoring homogeneous deformation. Here, we propose a competition strategy that leverages configurational entropy and surface termination to controllably modulate the atomic ripple structure within Nb₂CTe_x-based MXenes. This chemical disorder releases the local in-plane strain induced by termination atoms with large ionic radii, thus enabling the regulation of out-of-plane atomic displacement. The deliberate design of the ripple structure regulates the dielectric relaxation time of the microscopic dipole in the electric field. Consequently, high-entropy MXenes deliver strong intensity of microwave absorption (−41.12 dB) and an absorption bandwidth of nearly 10 GHz, covering the S-, C-, and X-bands. This study establishes the relationship between atomic ripple structure, atomic strain, polarization relaxation, and dielectric properties, providing guidance for designing advanced MXenes materials for various applications.

The two-dimensional (2D) layered materials have been applied across diverse fields such as electronics^{1–3}, optoelectronics^{4–6}, energy storage^{7–9}, sensors¹⁰, catalysis^{11,12}, and electromagnetic interference shielding^{13–15}, because of their exceptional electroconductivity and versatile surface chemistries^{16–22}. Ripple texturing, which is an inherent feature of 2D layered materials, originates from the periodical displacement of atoms due to thermal fluctuation and strain profiles. Traditionally, both spontaneously and thermally generated strains have been utilized to control ripple orientation, wavelength, and amplitude, enabling strain-based 2D material electronics²³. It can effectively modify mechanical, magnetic, and electronic properties by introducing spatially varying potentials or effective magnetic fields^{24–26}. For instance, the randomly distributed ripples induce

spatially disordered charge density fluctuations in the graphene by the π - σ rehybridization, significantly improving charge transport characteristics²⁷. However, precisely controlling the ripple structure remains a significant challenge.

Two-dimensional transition metal carbonitrides (MXenes) have been actively studied as a burgeoning class of 2D materials with excellent metallic conductivity and an abundance of surface defects^{28–31}. Especially, incorporating large ionic radius termination atoms can produce ripple structures within MXenes' framework without the aid of additional fields³², which is expected to effectively customize electronic properties. Notably, as promising electromagnetic (EM) shielding and absorption materials, most research has focused on interlayer engineering, defect strategy, and composite

¹Laboratory of Advanced Materials, Shanghai Key Lab of Molecular Catalysis and Innovative Materials, Advanced Coatings Research Center of Ministry of Education of China, State Key Laboratory of Coatings for Advanced Equipment, Fudan University, Shanghai 200438, China. ²These authors contributed equally: Minmin Liu, Liting Yang, Zhengchen Wu. ✉e-mail: rcche@fudan.edu.cn

methods to optimize MXenes' properties^{33–37}. For instance, simultaneously tuning the interlayer spacing and surface termination of $Ti_3C_2T_x$ to improve impedance matching and enhance EM wave loss³⁸. Besides, the assembled double-shell MXene@Ni microspheres via a spheroidization strategy achieve the maximum synergistic effect of dielectric and magnetic constituents³⁹. However, to the best of our knowledge, the ripple-modulated engineering and corresponding mechanisms have never been reported. Additionally, the correlation between ripple structure and microwave absorption (MA) performance in MXenes needs to be elucidated to achieve repeatable manipulation.

Herein, we successfully introduce and modulate atomic ripple structure through a competition strategy between configurational entropy and surface termination within Nb_2CTe_x -based MXenes⁴⁰. Introducing -Te termination through the Lewis acidic molten salt etching method generates the local in-plane strain, yielding atomic ripple structure^{41,42}. Since complex concentrated solutions of multiple principal elements can modify local strain distribution, replacing ions at M sites with multiple hetero-metal-atoms induces the evolution of local in-plane strain, thereby achieving precise control of atomic ripple structure. The elaborate design of the periodic ripple structure modulates the relaxation time of the microscopic dipole (caused by charge accumulation on the interface between MXenes and paraffin) in the applied electric field, ensuring controlled regulation of the dielectric properties. As a result, $(TiVnNbTaZr)_2CTe_x$ exhibits satisfactory effective absorption bandwidth covering the full band from 2 to 12 GHz. This work furthers insight into our fundamental understanding of entropy increasing contributions to polarization relaxation processes, and paves a new way for the research of MXenes absorbers.

Results and discussion

Entropy-modulated periodic ripple structure in MXenes

By using a compositionally complex doping strategy, we successfully prepared the Nb_2AlC -based MAX phases, including medium-entropy $(TiNbTa)_2AlC$ and high-entropy $(TiVnNbTaZr)_2AlC$ (Supplementary Fig. 1). Equimolar metal elements (Ti, Ta, V, and Zr) were progressively introduced into the M position of Nb_2AlC , thereby increasing configurational entropy⁴⁰. The synthesized MAX phases with nearly identical X-ray diffraction (XRD) patterns indicate minimal structural fluctuation induced by metal element introduction. The sharp and intense diffraction peaks located at approximate 2θ angles of 12.94° (002), 25.86° (004), 33.54° (100), 34.17° (101), 38.96° (103), 42.81° (104), and 52.44° (106) match well with reported M_2AX phases (Supplementary Fig. 2)⁴¹. Subsequent conversion from MAX phase to MXenes was accomplished through a Lewis acid molten salt etching method, yielding medium and high entropy MXenes (Fig. 1a and Supplementary Fig. 3). These products show a typical accordion-like microstructure morphology with primary sizes ranging from 2–15 μm , suggesting MXenes formation (Supplementary Fig. 4). The inductively coupled plasma atomic emission spectroscopy (ICP-AES) data determine the chemical formula $(Ti_{0.42}Nb_{0.30}Ta_{0.28})_2CTe_x$ and $(Ti_{0.26}V_{0.15}Nb_{0.22}Ta_{0.22}Zr_{0.15})_2CTe_x$, abbreviated as $(TiNbTa)_2CTe_x$ and $(TiVnNbTaZr)_2CTe_x$ (Supplementary Fig. 5 and Supplementary Table 1). The disappearance of diffraction peaks and the shift of (002) peaks to lower Bragg angles in the XRD patterns (Fig. 1b) (for Nb_2CTe_x , $(TiNbTa)_2CTe_x$, and $(TiVnNbTaZr)_2CTe_x$) confirm the complete transformation from MAX to MXenes phase. The above results are further corroborated by an atomic high-angle annular dark field (HAADF) scanning transmission electron microscopy (STEM) images of MXenes (Supplementary Fig. 6), where the center-to-center interlayer distance is calculated to be ~ 3.0 Å, almost in agreement with the value of 3.2 Å measured with XRD. Each M_2CTe_x monolayer (M=Nb, TiNbTa, TiVnNbTaZr) consists of four atomic layers: the middle two layers of M site atoms and the outer two layers of -Te terminations. To investigate the elemental distribution in the MXenes, atomic-resolved energy-dispersive X-ray spectroscopy (EDS) mapping for Nb_2CTe_x

(Supplementary Fig. 7), $(TiNbTa)_2CTe_x$ (Supplementary Fig. 8), and $(TiVnNbTaZr)_2CTe_x$ (Fig. 1c) was performed. The metal elements (Ti, V, Nb, Ta, and Zr) were found to occupy M sites, while Te atoms uniformly distribute on the surface of MXenes, demonstrating the replacement of Nb with the introduced metal atoms at the M sites. Moreover, all metal elements exhibit clear and periodic distributions corresponding to the atomic layer structure (Supplementary Fig. 7, Supplementary Fig. 8, and Fig. 1c), highlighting the uniform coexistence of introduced elements and Nb at the M sites. To better visualize compositional fluctuation, EDS profiles acquired along [001] direction were plotted. These profiles clearly demonstrate a homogeneous atomic distribution in the high entropy MXenes, where -Te terminations and metal elements are uniformly located at the T and M sites, respectively. These results substantiate the synthesis of Nb_2CTe_x -based medium and high entropy MXenes with high purity and homogeneity through the progressive introduction of metal elements into the M position of Nb_2AlC .

To evaluate the microstructure of MXenes phases, we acquired selected-area electron diffraction (SAED) patterns along the [100] zone axis. In contrast to the simulat SAED of Nb_2CTe_x (Supplementary Fig. 9), the synthesized Nb_2CTe_x MXenes have an additional set of diffraction spots (Fig. 1d) at the locations corresponding to $\frac{1}{6}[010]$, indicating the additional or increased chemical order. The intensity of these extra diffraction spots tends to decrease with the introduction of metal elements. For $(TiVnNbTaZr)_2CTe_x$, only faint additional diffraction information could be detected under the [100] zone axis. Apparently, the intensity of these extra diffraction spots, which are sensitive to the local atomic environment, can serve as an index to quantitatively evaluate the degree of superstructure. The normalized intensity of extra diffraction versus the number of elements in the M site is plotted in Fig. 1e and Supplementary Fig. 10, depicting a degradation in diffraction intensity with increasing the number of introduced elements. The linear response demonstrates that entropy-modulated atomic structures in MXenes are indeed plausible.

To directly investigate the atomic structure, the HAADF lattice images were acquired in STEM experiments. The Nb_2CTe_x MXenes show a characteristic periodic atomic ripple structure (Supplementary Fig. 6a), which may be attributed to the lattice strains induced by large Te atoms (ionic radius = 221 pm)³⁹. To confirm this hypothesis, Cl-terminated MXenes Nb_2CCl_x was synthesized using a different Lewis acid molten salt. In sharp contrast, Nb_2CCl_x does not exhibit a periodic ripple structure (Supplementary Fig. 11). Besides, X-ray photoelectron spectroscopy (XPS), and electron energy loss spectroscopy (EELS) for Nb_2CTe_x have been provided to exclude the influence of -O, -OH terminations on the ripple structure during the washing process (Supplementary Fig. 12, Supplementary Fig. 13, and Supplementary Table 2). As the increase of entropy, these ripple structure gradually diminishes, nearly disappearing in $(TiVnNbTaZr)_2CTe_x$ (Supplementary Fig. 6b and 6c). These results suggest that the extra diffraction spots in SAED patterns stem from the ripple structure. Furthermore, the corresponding FFT patterns ([100] zone axis) are shown in Supplementary Fig. 14, which also exhibit extra diffraction spots (circled in yellow). Meanwhile, a high-resolution lattice image-based method was applied, transitioning from the fast Fourier transform (FFT) patterns to inverse FFT (IFFT) images (Fig. 1f (ii), Fig. 1g (ii) and Fig. 1h (ii)). Superimposing the HAADF and IFFT images highlights the atomic ripple structure even more clearly, as it adds intensity to the MXenes columns (Fig. 1f (iii), Fig. 1g (iii), and Fig. 1h (iii)). By integrating SAED patterns, HAADF images, and IFFT images, we exhibit the evolutions of ripple structure in Nb_2CTe_x -based MXenes. Notably, the intensity and location of these extra diffraction spots in SAED patterns correlated to the amplitude intensity (AI) and wavelength of the atomic ripple structure, respectively. Hence, AI_x (note: x representative extra diffraction spots intensity) was proposed to quantitatively evaluate the ripple feature in MXenes, in which $AI_{0.0423}$ corresponds to Nb_2CTe_x , $AI_{0.0174}$ to $(TiNbTa)_2CTe_x$, and $AI_{0.0033}$ to $(TiVnNbTaZr)_2CTe_x$. Additionally, the

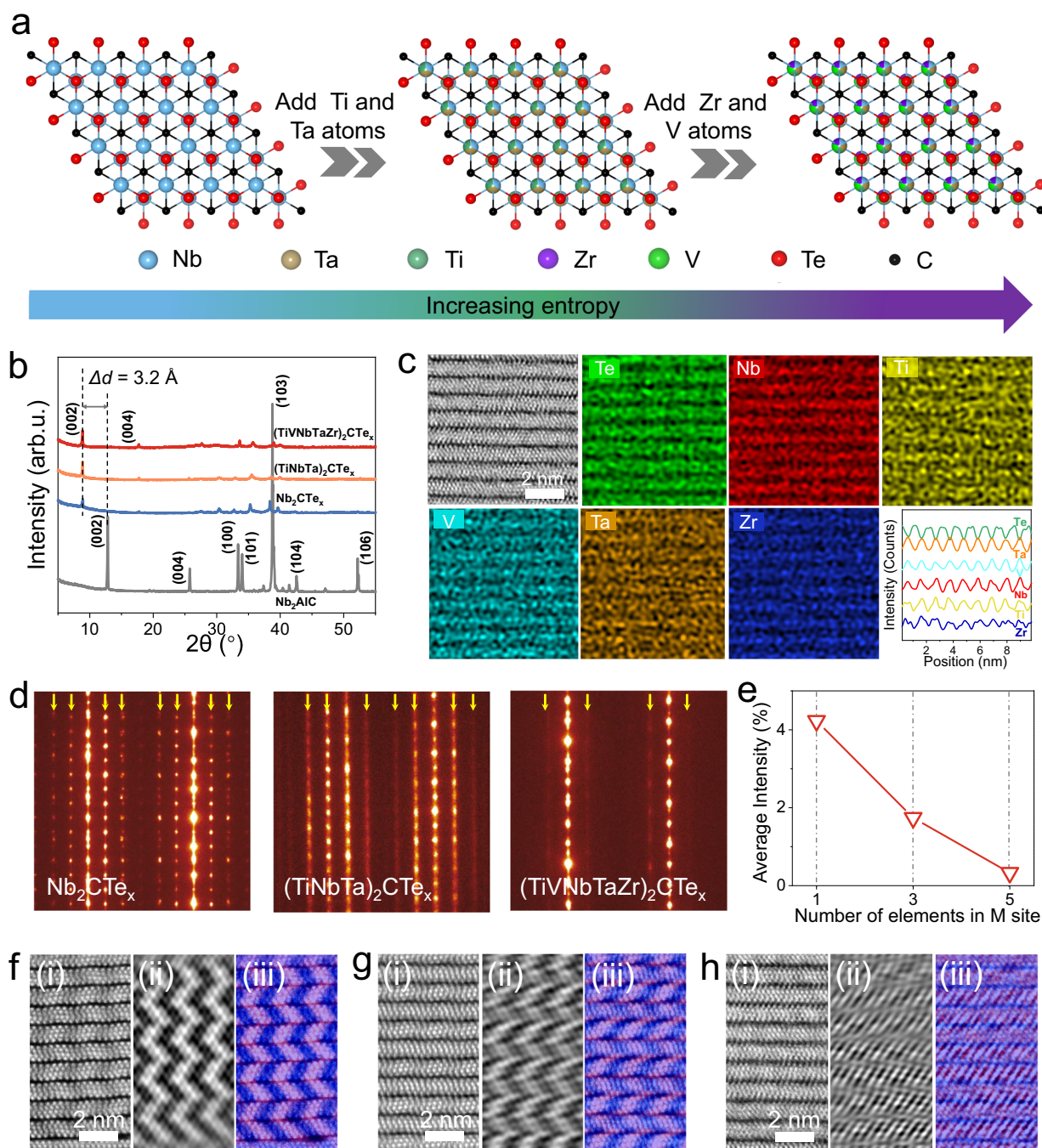


Fig. 1 | Entropy-modulated periodic ripple superstructure in MXenes.

a Schematic lattice structure of the MXenes with increasing entropy along the [001] zone axis. **b** X-ray diffraction (XRD) pattern of MAX phase and derived MXenes. **c** Atomically resolved elemental mappings of $(\text{TiVNbTaZr})_2\text{CTe}_x$, including atomic resolution high-angle annular dark-field (HAADF) image, individual distribution of Te, Nb, Ti, V, Ta, Zr, and corresponding energy dispersive spectroscopy (EDS) line profiles along the [001] direction. **d** Selected area electron diffraction (SAED) patterns for Nb_2CTe_x , $(\text{TiNbTa})_2\text{CTe}_x$, and $(\text{TiVNbTaZr})_2\text{CTe}_x$ along the [100] zone axis. The yellow arrows mark the location of the extra discs. **e** Dependence of normalized

diffraction intensity on the number of elements in the M site. **f-h** Atomic resolution high-angle annular dark-field (HAADF) images, inverse fast Fourier transform (IFFT) images obtained from the extra discs (the corresponding fast Fourier transform patterns with yellow solid circles marking the extra discs are shown in Supplementary Fig. 14), and the overlapped maps of atomic resolution high-angle annular dark-field (HAADF) and inverse fast Fourier transform (IFFT) images (**f** Nb_2CTe_x , **g** $(\text{TiNbTa})_2\text{CTe}_x$, **h** $(\text{TiVNbTaZr})_2\text{CTe}_x$). Source data are provided as a Source Data file.

location of extra diffraction spots shows a small change, with increasing configurational entropy. This indicates that the introduction of metal elements results in a slight fluctuation of ripple wavelength, maintaining an average value of approximately -1.77 nm.

To provide a more comprehensive description of the ripple spatial distribution, we also conducted atomic structure characterization along the [120] and [001] zone axes (Supplementary Fig. 15). The SAED

patterns acquired along the [120] zone axis exhibit extra diffraction discs at the locations corresponding to $\frac{1}{3}\{2\bar{1}0\}$. The corresponding HAADF images, IFFT images, and overlapped maps of HAADF and IFFT images further confirm the presence of the ripple structure of Nb_2CTe_x . Combined with the SAED results for [001] zone axis, which show additional spots corresponding to $\frac{1}{6}\{010\}$, the spatial distribution of these ripples correlates with the metal atom positions as the sample is rotated around

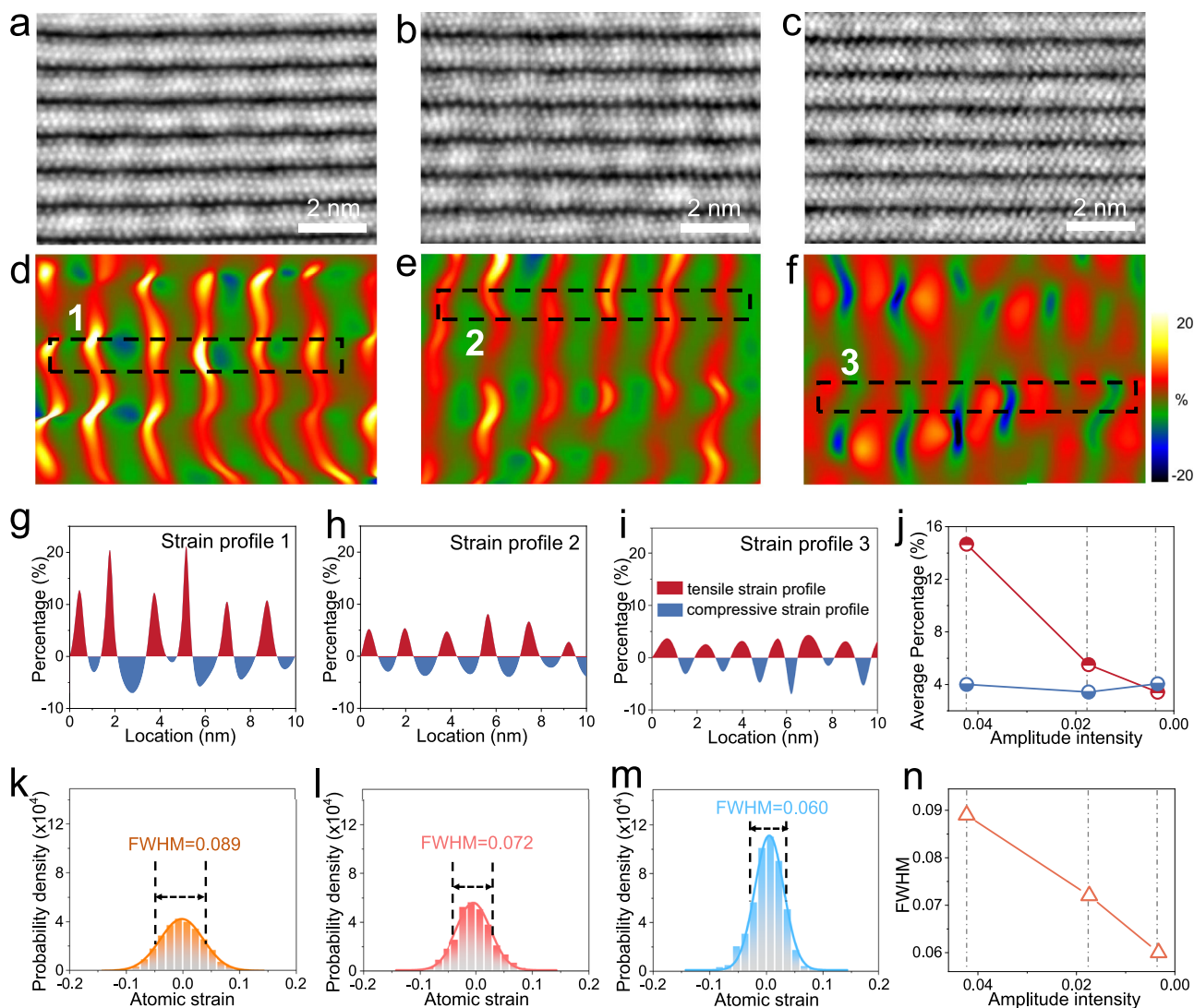


Fig. 2 | Strain analysis of periodic ripple superstructure of Nb_2CTe_x , $(\text{TiNbTa})_2\text{CTe}_x$, and $(\text{TiVnNbTaZr})_2\text{CTe}_x$. **a–c** Atomic resolution integrated differential phase contrast (iDPC) images of Nb_2CTe_x , $(\text{TiNbTa})_2\text{CTe}_x$, and $(\text{TiVnNbTaZr})_2\text{CTe}_x$, respectively. **d–f** Geometric phase analysis (GPA) of the atomic resolution integrated differential phase contrast (iDPC) (corresponding to **a–c**) data reveals the in-plane strain ϵ_{xx} mappings of Nb_2CTe_x , $(\text{TiNbTa})_2\text{CTe}_x$, and $(\text{TiVnNbTaZr})_2\text{CTe}_x$. The color from green to dark blue represents the compressive strain degree while the color from red to bright yellow refers to the tensile strain degree in the data bar. **g–i** Corresponding line profiles of areas 1, 2, and 3 (labeled in

d–f). **j** Dependence of average strain on the amplitude intensity (AI) of the ripple structure. The red semicircle represents the tensile strain and the blue semicircle indicates the compressive strain. **k–m** The statistical distribution obtained from the atomic-strain mappings. The orange, red, and blue curves are Gaussian fits of the atomic-strain probability density results for the Nb_2CTe_x , $(\text{TiNbTa})_2\text{CTe}_x$, and $(\text{TiVnNbTaZr})_2\text{CTe}_x$, respectively. The full width at half maximum (FWHM) of each curve represents the fluctuation degree of the atomic strain in the corresponding sample. **n** Dependence of full width at half maximum (FWHM) on the amplitude intensity (AI) of the ripple structure. Source data are provided as a Source Data file.

the c-axis. These findings suggest that the ripple structure takes on an island configuration arranged in a hexagonal pattern. To directly assess the ripple distribution, SAED patterns were also acquired along the [001] zone axis, further confirming the hexagonal arrangement. Additionally, HAADF images and corresponding IFFT images highlight the island configuration of the ripples, with an average size of -0.52 nm. Collectively, the results from SAED, HAADF, and IFFT analyses provide compelling evidence for the spatial distribution of ripple structures in the form of hexagonally arranged islands.

The mechanism of entropy-modulated atomic ripple structure in MXenes

To unveil the mechanism of entropy control ripple structure and realize repeatable manipulation of ripple in MXenes, we employed a combination of atomic resolution integrated differential phase contrast (iDPC) and the image processing technique of geometric phase

analysis (GPA), enabling atomic strain analysis with high accuracy and reliability⁴³. As shown in Fig. 2a–c, the iDPC images further confirm that the atomic ripple structure diminishes with increasing entropy, consistent with the results of the above SAED and HAADF characterization. Based on these iDPC images, subsequent nanoscale strain analysis within MXenes was accomplished through the GPA method, yielding the in-plane strain ϵ_{xx} (Fig. 2d–f) and out-of-plane strain ϵ_{yy} (Supplementary Fig. 16)⁴⁴. For Nb_2CTe_x MXenes, the ϵ_{xx} map clearly shows periodic and alternating compressive strain and tensile strain along *a* direction, corresponding to the periodic ripple structure. In contrast, the ϵ_{yy} map exhibits a random distribution. This result indicates that the periodic ripple structure arises from the nanoscale in-of-plane stress which is induced by large Te atoms. In sharp contrast, the nanoscale strain concentration phenomenon was not observed in the Nb_2Cl_x (Supplementary Fig. 17), further confirming the Te-termination-induced atomic ripple structure.

As introducing hetero-metal-atoms into M sites, random local strain arising from the unmatched atomic size and mass leads to diminution of alternating compressive strain and tensile strain, implying that increasing entropy can effectively release the nanoscale in-plane strain (Fig. 2e, f). To more intuitively and quantitatively analyze the entropy-induced evolution of stress distribution, the line profiles of areas 1, 2, and 3 (located in Fig. 2d–f) were plotted in Fig. 2g–i. For Nb₂CTe_x, the average tensile strain is 14.67%, which is extremely large compared to the average compressive strain −4.01%. Additionally, MXenes undergo significant degradation in tensile strain with the increased entropy, while the compressive stress remains relatively unchanged (Fig. 2j). This finding demonstrates that the periodic ripple structure is attributed to the nanoscale in-of-plane tensile strain and can be controlled through entropy-modulated tensile strain. Moreover, the statistical result of strain distribution is presented in Fig. 2k–m. The full width at half maximum (FWHM) of Nb₂CTe_x, (TiNbTa)₂CTe_x, and (TiVNbTaZr)₂CTe_x is 0.089, 0.072, and 0.060, respectively, indicating the fluctuation degree of the atomic-strain gradually decrease^{45,46}. The reduced FWHM value further proves that the in-of-plane tensile stress gradually decreases with the increase of entropy (Fig. 2n). Our results suggest that the uniform introduction of -Te termination causes local deformation, which generates the periodic strain in Nb₂CTe_x. Subsequently, the in-of-plane tensile strain is released through entropy increase, thereby leading to the adjustment of atomic ripple structure.

The ripple structure-interatomic coupling-electrical property correlation

To gain a more profound understanding of how this ripple structure affects the atomic electric fields and charge density distribution, we performed the differential phase contrast scanning transmission electron microscopy (DPC-STEM) technology⁴⁷. This technique can directly visualize the relative direction and strength of the electric field at each atomic column, pointing outwards from the center of the atomic columns⁴⁸. Figure 3a–c show the DPC images of Nb₂CTe_x, (TiNbTa)₂CTe_x, and (TiVNbTaZr)₂CTe_x, where the color and intensity correspond to the relative direction and strength of the electric field at each position. For Nb₂CTe_x, the introduction of Te induces an asymmetric electric field distribution within these disks (highlighted by orange ovals in Fig. 3d), indicating charge redistribution. With the entropy-modulated weakening of the periodic ripple structure, these disks suffer from distortion (Fig. 3d, the enlarged maps of areas 2#, and 3#), and the electric fields of adjacent atomic columns fuse, (TiVNbTaZr)₂CTe_x exhibits remarkable interatomic coupling. The results of DPC analysis indicate that the regulation of the ripple structure enhances the interatomic coupling electric field (Te-Te, Te-M site, and M-M site) within (TiNbTa)₂CTe_x, and (TiVNbTaZr)₂CTe_x, facilitating the transfer of electrons and cause the increase of the in-plane conductivity. Moreover, the actual conductivity was measured using the four-point probe method, in which the four-electrode devices were fabricated via focused ion beam (FIB) technology (Fig. 3i and Supplementary Fig. 18). The conductivities of Nb₂CTe_x, (TiNbTa)₂CTe_x, and (TiVNbTaZr)₂CTe_x is $0.61 \times 10^3 \text{ S} \cdot \text{m}^{-1}$, $1.60 \times 10^3 \text{ S} \cdot \text{m}^{-1}$, and $2.00 \times 10^3 \text{ S} \cdot \text{m}^{-1}$, respectively. The increase in actual conductivity further corroborates the above DPC results.

Density functional theory (DFT) calculations were conducted to investigate the local charge density distribution and transportation of Te with adjacent M site atoms. The 2D electron density difference mappings (Fig. 3e–g) were obtained by slicing along (100) crystal faces from the three-dimensional isosurface (Supplementary Fig. 19). As shown in Fig. 3e, the -Te surface terminal functionalities caused the charge density redistribution, where the electrons transfer from Te to Nb. The addition of foreign atoms to the M site of Nb₂CTe_x increases atomic distortion and local inhomogeneity⁴⁰, intensifying the interatomic coupling effect at Te-Te, Te-M sites, and M-M sites (Fig. 3f, g),

which is consistent with the experimental results of DPC. The density of states (DOS) is essentially the number of different states that an electron is allowed to occupy at a particular energy level, and a high DOS near the Fermi level means that there are more electron states available for the electron to occupy, thereby increasing the transition probability and conductivity of the electron^{34,47}. Due to the difference in the number of valence electrons and atoms for the simulation units, we performed the normalization of DOS value relative to valence electron number and atoms number for each simulation model (Nb₂CTe_x, (TiNbTa)₂CTe_x, and (TiVNbTaZr)₂CTe_x). The normalized DOS value increases with the increase of M-position entropy (Fig. 3h, Supplementary Table 3), indicating the enhanced electrical conductivity, which agrees with the trend of actually measured one.

Effects of entropy-modulated ripple structure on dielectric properties and microwave absorption performances

To clarify the correlation between the ripple structure and dielectric properties within MXenes, the electromagnetic parameters were measured using the coaxial method. The complex permittivity of Nb₂CTe_x, (TiNbTa)₂CTe_x, and (TiVNbTaZr)₂CTe_x ranging from 2 to 12 GHz were displayed in Fig. 4a–c, respectively. Obviously, the dielectric spectrum reflects two trends. First, both the ϵ' and ϵ'' values remarkably increase with the ripple structure weakening, this can be attributed to the strengthened in-plane conductivity discussed above. The second trend is the shift in the peak frequency of polarization. It is commonly believed that the relaxation time τ is an index of dipole mobility in dielectric materials, which is closely related to the polarization mechanism and is one of the key reasons for the dielectric loss of materials. According to the formula:

$$\tau = \frac{1}{\omega_c} = \frac{1}{2\pi f_c} \quad (1)$$

We obtain that the relaxation time τ is inversely proportional to the relaxation frequency f_c . As shown in the Cole-Cole curves in Fig. 4d and Supplementary Fig. 20, apparent Cole-Cole semicircles correspond to the polarization relaxation processes. Obviously, with the decrease in periodic ripple amplitude intensity, the relaxation frequency range gradually shifts to the lower frequency, corresponding to the increase in relaxation time. This can be explained by the microscopic dipole model, in which the charges accumulate on the interfaces between MXenes and paraffin wax under an applied electric field, forming microscopic dipoles. After changing the direction of the external electric field, the positive and negative charges that accumulate on the interfaces between MXenes and paraffin are slowly redistributed, and the microscopic dipoles are flipped, resulting in relaxation time. For Nb₂CTe_x, (TiNbTa)₂CTe_x, and (TiVNbTaZr)₂CTe_x, the out-of-plane conductivity decreases with the entropy-modulated periodic ripple structure weakening (from $17.48 \text{ S} \cdot \text{m}^{-1}$, $9.45 \text{ S} \cdot \text{m}^{-1}$, to $2.33 \text{ S} \cdot \text{m}^{-1}$) (Supplementary Figs. 21 and 22). Hence, under the external electric field, the reduced out-of-plane conductivity slows down the redistribution of positive and negative charges in the microscopic dipole, resulting in prolonged polarization relaxation time.

The maximum value of reflection loss (RL_{max}) and effective absorption bandwidth (EAB, the bandwidth of $RL \leq -10 \text{ dB}$), serving as two key factors for microwave absorption (MA), were further investigated⁴⁹. As summarized in Fig. 4e, the RL_{max} values located at 8.8 GHz, 8.48 GHz, and 6.88 GHz correspond to dielectric relaxation peaks (Fig. 4a–c) for Nb₂CTe_x, (TiNbTa)₂CTe_x, and (TiVNbTaZr)₂CTe_x, respectively. (TiVNbTaZr)₂CTe_x exhibits the RL_{max} value of −41.12 dB at a thickness of only 2.3 mm (Supplementary Fig. 23), a notable improvement compared with the −26.10 dB of Nb₂CTe_x. Figure 4f shows the dependency of EAB on the amplitude intensity of the ripple structure. In the 2–12 GHz range, there are only two extremely narrow EABs the

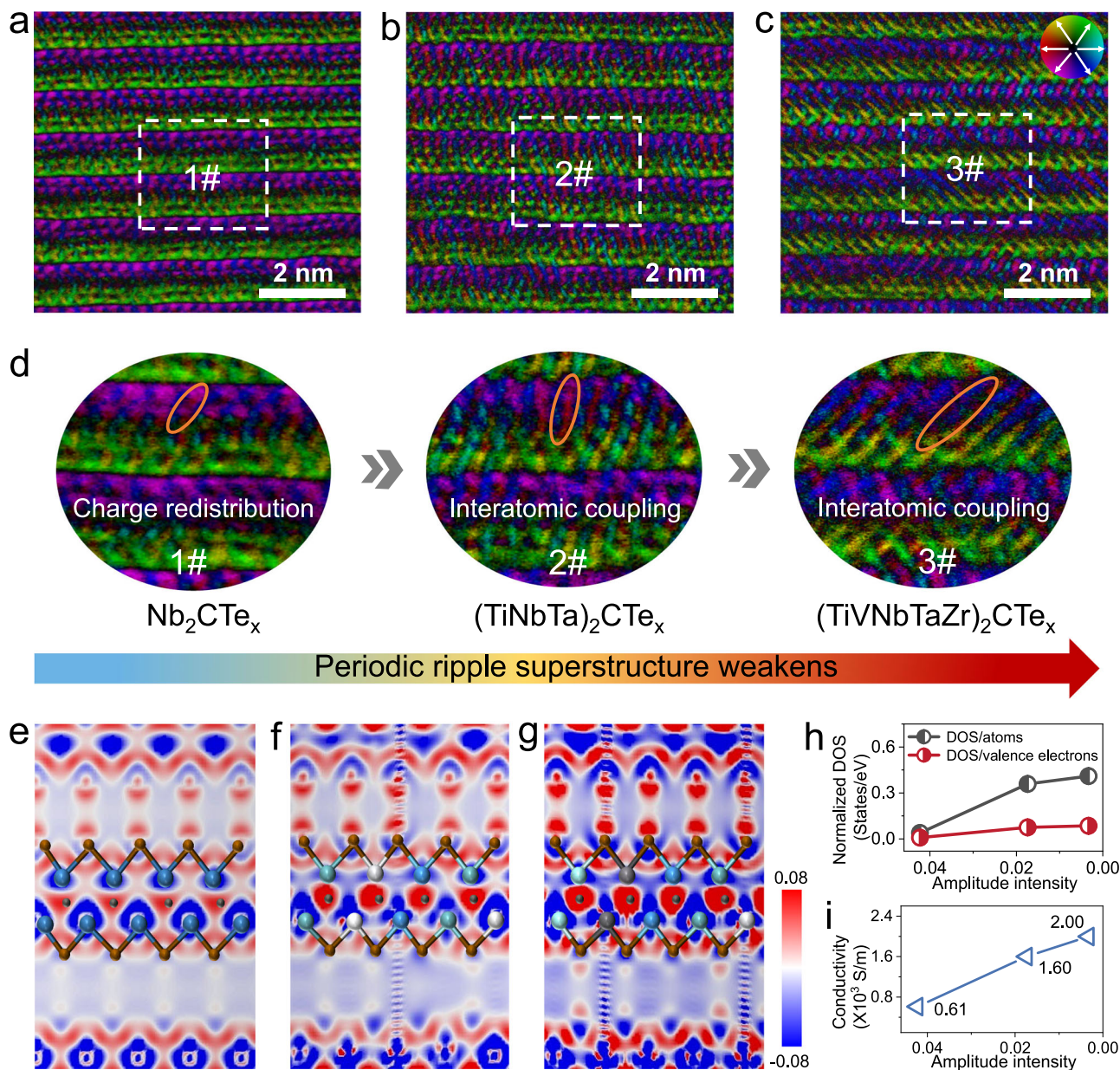


Fig. 3 | Differential phase contrast (DPC) characterization results and density functional theory (DFT) calculations of MXenes. a–c Differential phase contrast (DPC) images of Nb_2CTe_x , $(\text{TiNbTa})_2\text{CTe}_x$, and $(\text{TiVNbTaZr})_2\text{CTe}_x$ along the [100] zone axis, showing electric field vector mapping. The color wheel indicates how color and shade denote the electric field relative orientation and relative strength. **d** Enlarged regions of areas 1#, 2#, and 3# (labeled in a–c). The orange ovals indicate the asymmetric electric field distribution and interatomic coupling. **e–g** The charge density difference between the M sites and -Te termination (**e** Nb_2CTe_x ,

f $(\text{TiNbTa})_2\text{CTe}_x$, and **g** $(\text{TiVNbTaZr})_2\text{CTe}_x$). The red area represents electron accumulation and the blue area represents electron consumption. The blue, dark green, light gray, dark gray, light green, brown, and black represent atoms Nb, Ti, Ta, V, Zr, Te, and C, respectively. **h** Dependency of normalized density of states (DOS) on amplitude intensity (AI) of the ripple structure. **i** Dependency of in-plane conductivity on amplitude intensity (AI) of the ripple structure. Source data are provided as a Source Data file.

corresponding thicknesses are 2.5 mm and 3.0 mm for Nb_2CTe_x . By contrast, the EAB of $(\text{TiVNbTaZr})_2\text{CTe}_x$ covers the S-band, C-band, and X-band by adjusting the coating thickness from 1.5 to 5.5 mm (Supplementary Fig. 24), highlighting the excellent absorption capability. These results demonstrate that the MA performances of MXenes can be controlled by entropy-modulated periodic ripple structure.

In conclusion, the entropy-increasing strategy precisely controls the atomic ripple structure in MXenes, and a mechanistic link between the atomic ripple structure and macro-properties is established. Introducing multiple metallic atoms into the M site results in the increase of configurational entropy, which gradually mitigates the

local in-plane strain, achieving the precise modulation of atomic ripple structure. Moreover, the diminished out-of-plane conductivity impedes the redistribution of positive and negative charges within the microscopic dipole under an external electric field, thereby extending the polarization relaxation time and facilitating the directional polarization ability of MXenes. As a result, the synthesized $(\text{TiVNbTaZr})_2\text{CTe}_x$ exhibits preminent MA performances, including an RL_{max} value of -41.12 dB and the EAB covering the S-band, C-band, and X-band. Our results broaden the perspective for entropy engineering to regulate macro-properties, furthering the development of MXenes-based devices.

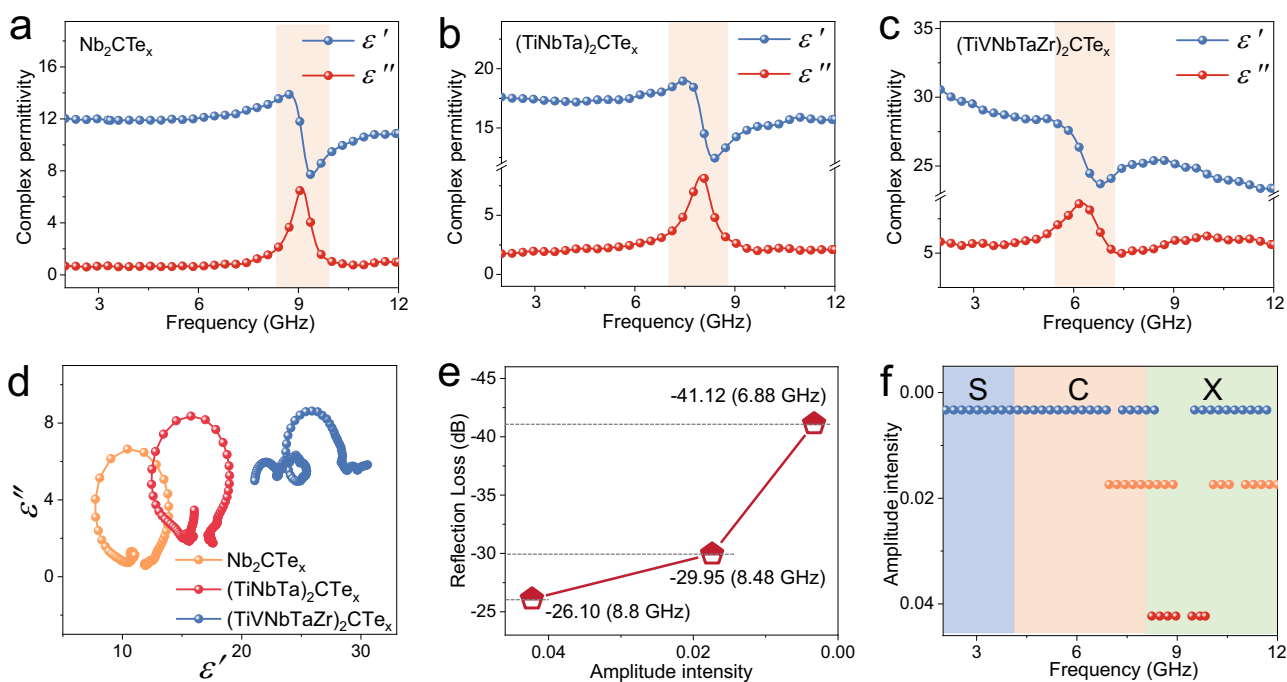


Fig. 4 | Electrical properties and microwave absorption performances of MXenes. a–c Complex permittivity of Nb_2CTe_x , $(\text{TiNbTa})_2\text{CTe}_x$, and $(\text{TiVNbTaZr})_2\text{CTe}_x$, respectively. **d** Cole-Cole curves. **e** Maximum reflection loss

(RL_{max}) diagram. **f** Dependency of effective absorption bandwidth (EAB) on amplitude intensity (AI) of the ripple structure. Source data are provided as a Source Data file.

Methods

Chemicals and materials

High-purity commercial powders of Ti (<1 μm , 99.8 wt.%), V (10–20 μm , 98 wt.%), Nb (<10 μm , 99.8 wt.%), Ta (<10 μm , 99.5 wt.%), Zr (<10 μm , 99.8 wt.%), and aluminum (1 μm , 99 wt.%) were all purchased from Shanghai Pantian Nano Material Co., Ltd. CuI (anhydrous, 99.99%), KI (anhydrous, 99.99%), and Te powder (300 mesh, 99.9%) were purchased from Sinopharm Chemical Reagent Co., Ltd. HCl (36–38%), $(\text{NH}_4)_2\text{S}_2\text{O}_8$ (>98 wt.%), and $\text{NH}_3\cdot\text{H}_2\text{O}$ (25%–28%), were purchased from Aladdin.

Synthesis of MAX phase

The starting materials with a stoichiometric ratio of M: Al: C = 2:1.1:1 (the elements in M-site were equimolar) were mixed in an agate mortar. Notably, Al powder, which has a low melting point of 660 $^\circ\text{C}$, was added in excess to compensate for loss during the reaction. Ethanol was added and the mixture was grained for 40 min. Subsequently, the mixture powders were placed in an alumina crucible and heated in a tube furnace at 1500 $^\circ\text{C}$ for 2 h under an Ar atmosphere (at a heating rate of 5 $^\circ\text{C min}^{-1}$). After cooling to room temperature, the synthesized MAX product was washed with HCl. Finally, the target product (Nb_2AlC , $(\text{TiNbTa})_2\text{AlC}$, and $(\text{TiVNbTaZr})_2\text{AlC}$) were obtained.

Synthesis of multilayer MXenes

The Lewis acid molten salt method was employed to transform from MAX into MXenes. Briefly, the MAX phases (Nb_2AlC , $(\text{TiNbTa})_2\text{AlC}$, and $(\text{TiVNbTaZr})_2\text{AlC}$), CuI, Te, and KI were thoroughly ground using a mortar under argon protection in a glove box. The prepared mixture powder was then transferred to an alumina crucible and loaded into a tube furnace, where it was heat-treated at 700 $^\circ\text{C}$ for 7 h under an Ar atmosphere. After the reaction, the products were removed from the furnace and washed with $\text{NH}_3\cdot\text{H}_2\text{O}$, $(\text{NH}_4)_2\text{S}_2\text{O}_8$ to remove the residual CuI and by-product Cu. Finally, the target MXenes (Nb_2CTe_x , $(\text{TiNbTa})_2\text{CTe}_x$, and $(\text{TiVNbTaZr})_2\text{CTe}_x$) were obtained.

DFT methods

The density functional theory (DFT) calculations were performed by using the Cambridge Sequential Total Energy Package (CASTEP), which the version was MS CASTEP 2017. The generalized gradient approximation (GGA) of the Perdew-Burke-Ernzerhof (PBE) function was employed in this investigation. The electron wave function is expanded by a plane wave basis with a kinetic energy cutoff of 400 eV. The K-points mesh was set to $3 \times 3 \times 1$. The supercell was set as $3 \times 6 \times 2$ to construct the models in Fig. 3e–g using the initial primitive cell of MXenes. The numbers of atoms for Nb_2CTe_x , $(\text{TiNbTa})_2\text{CTe}_x$, and $(\text{TiVNbTaZr})_2\text{CTe}_x$ supercell were 120, 120, and 192, respectively (The specific number of each atom is listed in Supplementary Table 4). We used a script to generate a randomly distributed model with Ti, V, Ta, and Zr atoms replacing part of Nb. For Nb_2CTe_x , the ratio in the M position for Nb was set as 100%. The M-site composition for $(\text{TiNbTa})_2\text{CTe}_x$ was set to 33.33% each for Ti, Nb, and Ta. For $(\text{TiVNbTaZr})_2\text{CTe}_x$, the M-site composition was set to 20% each for Ti, V, Nb, Ta, and Zr. Ultimately, the various M position atoms were randomly distributed in the same proportion in $(\text{TiNbTa})_2\text{CTe}_x$ and $(\text{TiVNbTaZr})_2\text{CTe}_x$. The energy tolerance was set as 2×10^{-5} eV and the force tolerance was set as 0.05 eV $\cdot \text{\AA}^{-1}$. The normalized DOS value was calculated by the normalization of DOS towards valence electrons to evaluate the electrical properties of the models.

Material characterization

The crystalline architecture of the MAX phase and MXene was characterized using Powder X-ray diffraction (XRD, Bruker, D8-Advance X-ray diffractometer, Germany) with Ni-filtered Cu K α radiation at a scan rate of 2 $^\circ$ /min. The composition ratio of M-position elements within $(\text{TiNbTa})_2\text{CTe}_x$ and $(\text{TiVNbTaZr})_2\text{CTe}_x$ was determined by a PE-8000 inductively coupled plasma atomic emission spectroscopy (ICP-AES). The surface chemical composition and chemical state of the Nb_2CTe_x were obtained on a KRATOS Axis Ultra DLD equipped with a monochromatic X-ray source. Morphological investigations were conducted using field-emission scanning electron microscopy (Hitachi S-4800,

Japan) operated at 5 kV. Specimen preparation for SAED, TEM, HRTEM images, STEM-EDS, STEM-iDPC, and STEM-HAADF measurements were performed using a dual-beam focused ion beam microscopy operating at 2–30 kV (ThermoFisher Scientific, Helios G4 CX, American). Following the standard FIB sample preparation technique, the specimen thickness for acquiring high-resolution STEM images should be less than 50 nm with approximately 1 nm-thick surface-damaged layer. The atomic TEM and STEM experiments were carried out on a dual spherical aberration correction field-emission STEM (ThermoFisher Scientific, Spectra 300 TEM, American) operated at 300 kV, equipped with STEM-iDPC detector, STEM-HAADF detector, and a Super-X EDS. To ensure a high signal-to-noise ratio, each EDS mapping at atomic resolution required approximately 0.5 h.

Conductivity measurements

The four-electrode devices were designed using focused ion beam (FIB) techniques to test the conductivity of MXenes in this work. The sample lamellas were installed on the nanochips, and four FIB-assisted superconducting Pt electrodes were fabricated by ion-beam-induced deposition, in which the outer electrode and the inner electrode are used to measure the current and voltage, respectively. Then the resistance R of MXenes was obtained based on Ohm's law. Subsequently, the conductivity σ was calculated according to the formula: $\sigma = L/(R \cdot a \cdot b)$, where L , a , and b are the length, width, and thickness between the voltage measurement points, where were obtained from the front view and top view SEM images.

Microwave absorption measurements

The as-obtained MXenes (Nb_2CTe_x , $(\text{TiNbTa})_2\text{CTe}_x$, and $(\text{TiVNbTaZr})_2\text{CTe}_x$) samples were immersed into the molten paraffin, mixed thoroughly and pressed into coaxial rings ($\phi_{\text{outer}} = 7.0$ mm; $\phi_{\text{inner}} = 3.0$ mm). The electromagnetic parameters with the frequency range of 2–12 GHz were measured by a network analyzer (Keysight, N5230C). Finally, the coaxial transmission line method was employed to calculate the reflection loss values:

$$RL = 20 \log \left| \frac{\sqrt{\mu_r/\epsilon_r} \tanh[j(2\pi f d/c) \sqrt{\mu_r \epsilon_r}] - 1}{\sqrt{\mu_r/\epsilon_r} \tanh[j(2\pi f d/c) \sqrt{\mu_r \epsilon_r}] + 1} \right| \quad (2)$$

where ϵ_r and μ_r are the electromagnetic parameters of complex permittivity and permeability, d is the specimen thickness, f is microwave frequency, and c is the speed of light velocity in a vacuum.

Data availability

Source data are provided in this paper. The data that support the findings of this study are available from the corresponding author upon request. The coordinate files in POSCAR format can be found in Supplementary Data [Coordinate files for electronic structure calculations]. Source data are provided with this paper.

References

- Xia, Y. et al. Thickness-independent capacitance of vertically aligned liquid-crystalline MXenes. *Nature* **557**, 409–412 (2018).
- Lee, H. J. et al. Hetero-dimensional 2D $\text{Ti}_3\text{C}_2\text{T}_x$ MXene and 1D graphene nanoribbon hybrids for machine learning-assisted pressure sensors. *ACS Nano* **15**, 10347–10356 (2021).
- Lee, G.-H. et al. Deep-learning-based deconvolution of mechanical stimuli with $\text{Ti}_3\text{C}_2\text{T}_x$ MXene electromagnetic shield architecture via dual-mode wireless signal variation mechanism. *ACS Nano* **14**, 11962–11972 (2020).
- Ying, G., Dillon, A. D., Fafarman, A. T. & Barsoum, M. W. Transparent, conductive solution processed spincast 2D Ti_2CT_x (MXene) films. *Mater. Res. Lett.* **5**, 391–398 (2017).
- Hantanasirisakul, K. et al. Fabrication of $\text{Ti}_3\text{C}_2\text{T}_x$ MXene transparent thin films with tunable optoelectronic properties. *Adv. Electron. Mater.* **2**, 1600050 (2016).
- Dillon, A. D. et al. Highly conductive optical quality solution-processed films of 2D titanium carbide. *Adv. Funct. Mater.* **26**, 4162–4168 (2016).
- Zhao, M.-Q. et al. Flexible MXene/carbon nanotube composite paper with high volumetric capacitance. *Adv. Mater.* **27**, 339–345 (2015).
- Lukatskaya, M. R. et al. Ultra-high-rate pseudocapacitive energy storage in two-dimensional transition metal carbides. *Nat. Energy* **6**, 17105 (2017).
- Ghidiu, M., Lukatskaya, M. R., Zhao, M.-Q., Gogotsi, Y. & Barsoum, M. W. Conductive two-dimensional titanium carbide 'clay' with high volumetric capacitance. *Nature* **516**, 78–90 (2014).
- Zhang, Y.-Z. et al. MXenes stretch hydrogel sensor performance to new limits. *Sci. Adv.* **4**, eaat0098 (2018).
- Abou Hamdan, M. et al. Supported molybdenum carbide and nitride catalysts for carbon dioxide hydrogenation. *Front. Chem.* **8**, 452 (2020).
- Figueras, M. et al. Supported molybdenum carbide nanoparticles as an excellent catalyst for CO_2 hydrogenation. *ACS Catal.* **11**, 9679–9687 (2021).
- Shahzad, F. et al. Electromagnetic interference shielding with 2D transition metal carbides (MXenes). *Science* **353**, 1137–1140 (2016).
- Iqbal, A. et al. Anomalous absorption of electromagnetic waves by 2D transition metal carbonitride Ti_3CNT_x (MXene). *Science* **369**, 446–450 (2020).
- Raagulan, K. et al. An effective utilization of MXene and its effect on electromagnetic interference shielding: flexible, free-standing, and thermally conductive composite from MXene-PAT-poly(*p*-aminophenol)-polyaniline co-polymer. *RSC Adv.* **10**, 1613–1633 (2020).
- Lukatskaya, M. R. et al. Probing the mechanism of high capacitance in 2D titanium carbide using in situ X-ray absorption spectroscopy. *Adv. Energy Mater.* **5**, 1500589 (2015).
- Xu, C. et al. Large-area high-quality 2D ultrathin Mo_2C superconducting crystals. *Nat. Mater.* **14**, 1135–1141 (2015).
- Miranda, A., Halim, J., Barsoum, M. W. & Lorke, A. Electronic properties of freestanding $\text{Ti}_3\text{C}_2\text{T}_x$ MXene monolayers. *Appl. Phys. Lett.* **108**, 033102 (2016).
- Hart, J. L. et al. Control of MXenes' electronic properties through termination and intercalation. *Nat. Commun.* **10**, 522 (2019).
- Zhang, T. et al. Simultaneously tuning interlayer spacing and termination of MXenes by Lewis-basic halides. *Nat. Commun.* **13**, 6731 (2022).
- Li, M. et al. $\text{Ti}_3\text{C}_2\text{T}_x/\text{MoS}_2$ Self-Rolling rod-based foam boosts interfacial polarization for electromagnetic wave absorption. *Adv. Sci.* **9**, 2201118 (2022).
- Deng, B. et al. Electrostatically self-assembled two-dimensional magnetized MXene/hollow Fe_3O_4 nanoparticle hybrids with high electromagnetic absorption performance and improved impedance matching. *J. Mater. Chem. A* **9**, 3500–3510 (2021).
- Bao, W. et al. Controlled ripple texturing of suspended graphene and ultrathin graphite membranes. *Nat. Nanotechnol.* **4**, 562–566 (2009).
- Rainis, D. et al. Gauge fields and interferometry in folded graphene. *Phys. Rev. B* **83**, 165403 (2011).
- Prada, E., San-Jose, P. & Brey, L. Zero Landau level in folded graphene nanoribbons. *Phys. Rev. Lett.* **105**, 106802 (2010).
- Bunch, J. S. et al. Electromechanical resonators from graphene sheets. *Science* **315**, 490–493 (2007).
- Kim, E.-A. & Castro Neto, A. H. Graphene as an electronic membrane. *Europhys. Lett.* **84**, 57007 (2008).

28. Mohammadi, A. V., Rosen, J. & Gogotsi, Y. The world of two-dimensional carbides and nitrides (MXenes). *Science* **372**, abf1581 (2021).
29. Chaudhari, N. K. et al. MXene: an emerging two-dimensional material for future energy conversion and storage applications. *J. Mater. Chem. A* **5**, 24564–24579 (2017).
30. Wang, H. et al. Clay-Inspired MXene-based electrochemical devices and photo-electrocatalyst: state-of-the-art progresses and challenges. *Adv. Mater.* **30**, 1704561 (2018).
31. Tapaszto, L. et al. Breakdown of continuum mechanics for nanometre-wavelength rippling of graphene. *Nat. Phys.* **8**, 739–742 (2012).
32. Ding, H. et al. Chemical scissor-mediated structural editing of layered transition metal carbides. *Science* **379**, 1130–1135 (2023).
33. Wu, N. et al. Dielectric properties and electromagnetism simulation of molybdenum disulfide and ferric oxide-modified $Ti_3C_2T_x$ MXene hetero-structure for potential microwave absorption. *Adv. Compos. Hybrid. Mater.* **5**, 1548–1556 (2022).
34. Wu, F. et al. Multifunctional MXene/C aerogels for enhanced microwave absorption and thermal insulation. *Nano-Micro Lett.* **15**, 194 (2023).
35. Gao, Y. et al. Engineering 2D MXene and LDH into 3D hollow framework for boosting photothermal energy storage and microwave absorption. *Small* **19**, 2303113 (2023).
36. Yun, T. et al. Electromagnetic shielding of monolayer MXene assemblies. *Adv. Mater.* **32**, 1906769 (2020).
37. Lee, G. S. et al. Maximized internal scattering in heterostack $Ti_3C_2T_x$ MXene/graphene oxide film for effective electromagnetic interference shielding. *2D Mater.* **10**, 035022 (2023).
38. Du, Y. et al. Balancing MXene surface termination and interlayer spacing enables superior microwave absorption. *Adv. Funct. Mater.* **33**, 2301449 (2023).
39. Wen, C. et al. High-density anisotropy magnetism enhanced microwave absorption performance in $Ti_3C_2T_x$ MXene@Ni microspheres. *ACS Nano* **16**, 1150–1159 (2022).
40. Yang, B. et al. Engineering relaxors by entropy for high energy storage performance. *Nat. Energy* **8**, 956–964 (2023).
41. Chen, L. et al. Multiprincipal element M_2FeC ($M = Ti, V, Nb, Ta, Zr$) MAX phases with synergistic effect of dielectric and magnetic Loss. *Adv. Sci.* **10**, 2206877 (2023).
42. Li, Y. et al. A general Lewis acidic etching route for preparing MXenes with enhanced electrochemical performance in non-aqueous electrolyte. *Nat. Mater.* **19**, 894–899 (2020).
43. Hytch, M., Houdellier, F., Hue, F. & Snoeck, E. Nanoscale holographic interferometry for strain measurements in electronic devices. *Nature* **453**, 1086–U1085 (2008).
44. Tang, Y. L. et al. Observation of a periodic array of flux-closure quadrants in strained ferroelectric $PbTiO_3$ films. *Science* **348**, 547–551 (2015).
45. Wang, L. et al. Tailoring planar slip to achieve pure metal-like ductility in body-centred-cubic multi-principal element alloys. *Nat. Mater.* **22**, 950–957 (2023).
46. Du, Z. et al. High-entropy atomic layers of transition-metal carbides (MXenes). *Adv. Mater.* **33**, 2101473 (2021).
47. Xu, J. et al. Atomic-level polarization in electric fields of defects for electrocatalysis. *Nat. Commun.* **14**, 7849 (2023).
48. Wang, W. et al. Direct atomic-scale structure and electric field imaging of triazine-based crystalline carbon nitride. *Adv. Mater.* **33**, 2106359 (2021).
49. Wu, Z. et al. Enhanced microwave absorption performance from magnetic coupling of magnetic nanoparticles suspended within hierarchically tubular composite. *Adv. Funct. Mater.* **29**, 1901448 (2019).

Acknowledgements

This work was supported by the National Natural Science Foundation of China (No. 12327804, 52231007, T2321003, 22088101, 22405050), the National Key Research Program of China (No. 2024YFA1208902, 2024YFA1408000, 2021YFA1200600), the Science and Technology Commission of Shanghai Municipality (No. 24ZR1406400), Aeronautical Science Foundation of China (No. 202400180P9001, 2024M0730P9001), Key Laboratory of High Temperature Electromagnetic Materials and Structure of MOE (No. KB202401), and Fund of Science and Technology on Surface Physics and Chemistry Laboratory (No. JCKYS2023120201).

Author contributions

R.C. conceived and designed the research. M.L., L.Y., and Z.W. contributed equally to this work. M.L. carried out the experiments, analyzed the data and wrote the manuscript. L.Y. performed the TEM test, analyzed the data and wrote the manuscript. Z.W. analyzed the data and wrote the manuscript. G.C. conducted the DFT calculations. X.W., X.Y., and G.L. help with the data analysis. All authors commented on the results and contributed to manuscript revisions. The corresponding authors: Renchao Che.

Competing interests

The authors declare no competing interests.

Additional information

Supplementary information The online version contains supplementary material available at <https://doi.org/10.1038/s41467-025-60890-3>.

Correspondence and requests for materials should be addressed to Renchao Che.

Peer review information *Nature Communications* thanks Jaekwang Lee and the other, anonymous, reviewer(s) for their contribution to the peer review of this work. A peer review file is available.

Reprints and permissions information is available at <http://www.nature.com/reprints>

Publisher's note Springer Nature remains neutral with regard to jurisdictional claims in published maps and institutional affiliations.

Open Access This article is licensed under a Creative Commons Attribution-NonCommercial-NoDerivatives 4.0 International License, which permits any non-commercial use, sharing, distribution and reproduction in any medium or format, as long as you give appropriate credit to the original author(s) and the source, provide a link to the Creative Commons licence, and indicate if you modified the licensed material. You do not have permission under this licence to share adapted material derived from this article or parts of it. The images or other third party material in this article are included in the article's Creative Commons licence, unless indicated otherwise in a credit line to the material. If material is not included in the article's Creative Commons licence and your intended use is not permitted by statutory regulation or exceeds the permitted use, you will need to obtain permission directly from the copyright holder. To view a copy of this licence, visit <http://creativecommons.org/licenses/by-nc-nd/4.0/>.

© The Author(s) 2025